Enhanced Photocurrent Generation from Indium-Tin-Oxide/Fe_2TiO_5 Hybrid Nanocone Arrays

Kai Chen[1,2*], Thang Duy Dao[1], Thien Duc Ngo[1,4], Hai Dang Ngo[1,4], Akemi Tamanai[1,5], Satoshi Ishii[1], Xiangping Li[2], Hiroaki Misawa[3], Tadaaki Nagao[1,4*]

[1]International Center for Materials Nanoarchitectonics, National Institute for Materials Science, Tsukuba, 305-0044, Japan

[2]Institute of Photonics Technology, Jinan University, Guangzhou, 510632, China

[3]Research Institute for Electronic Science, Hokkaido University N21, W10, CRIS Building, Kita-ku, Sapporo 001-0021, Japan

[4]Department of Condensed Matter Physics, Hokkaido University, Sapporo, 060-0808, Japan

[5]RIKEN Cluster for Pioneering Research, RIKEN, Wako, 351-0198, Japan

*NAGAO.Tadaaki@nims.go.jp; *kaichen@jnu.edu.cn

Abstract

Semiconductor oxide materials, including α-Fe_2O_3 (hematite), have been investigated as possible candidates for large-scale solar-to-chemical energy conversion. However, many of these materials suffer from inefficient charge transport leading to undesirable charge recombination. Although plasmon-enhanced photocatalysis has achieved some success in enhancing light absorption and hot carrier generation, the intrinsic ohmic losses within the metal hinder its wide applications. Here, we use large-area indium-tin-oxide (ITO) nanocone arrays that exhibit both high electrical transport, strong light trapping and enlarged surface area with reduced ohmic losses. We further adopted sputtered iron titanate (Fe_2TiO_5) thin films that show better photocatalytic performance than hematite. The photoanode made of all-oxide ITO/Fe_2TiO_5 nanocone array exhibited Mie resonance-enhanced photocurrent generation up to 31 times. These ITO nanocones can be readily combined with other oxide materials providing great opportunities for efficient photon management in enhanced photocatalysis.

Key words: Mie resonance, photocatalysis, iron titanate (Fe_2TiO_5), photocurrent, nanocone

1. Introduction

Solar-driven photocatalytic water splitting has huge potential for future green energy production.[1-3] A variety of semiconductor oxides, including TiO_2,[4-5] $BiVO_4$,[6-7] and Fe_2O_3,[8-10] have been demonstrated and widely investigated as potential photocatalytic materials for this purpose. Each type of oxide has exhibited promising potentials as photoanodes in photocatalytic water splitting. In particular, α-Fe_2O_3 (hematite) has drawn intensive attention due to its abundance, chemical stability and favorable bandgap structure for solar light absorption.[11-14] However, a major hurdle for the practical application of Fe_2O_3 is the mismatch between its electronic and photonic length scale as the charge carrier diffusion length is only a few nanometers while the light absorption length is on the order of tens of nanometers. The photogenerated carriers suffer from recombination losses that make no contribution to the water splitting process. The Fe_2O_3 photoanodes thus exhibit poor oxygen evolution reaction kinetics. In addition, the conduction band of Fe_2O_3 is below the reversible hydrogen potential. Thus, an electrical bias is required to provide hydrogen evolution. In this context, earth abundant iron titanates constitute another class of strong solar-light absorbers with wide spectral range. Pseudobrookite Fe_2TiO_5 shows a rare crystal structure similar to a lunar mineral *armalcolite* and has recently been reported either in hybrid or stand-alone thin films with better photocatalytic performance.[15-17] It is noted that the Fe_2TiO_5 thin films used in these reports are wet-chemically prepared and few reports exists on physical synthesis and in large scale. Because pseudobrookite-type mineral is known to be metastable at room temperature and has rather high structural anisotropy as well as anisotropic thermal expansion, special care is required for successful film growth. Sputter deposition can provide more flexibility and stability to the fabrication process and are also suitable for industry applications[18].

For both Fe_2O_3 and Fe_2TiO_5, short charge carrier diffusion length suggests that it is advantageous to apply them in the form of ultrathin films, which inadvertently results in less photon absorption inside the functional materials. Significant effort has been applied to tackle this problem including doping of Fe_2O_3 and integration with other oxides with limited success.[19-21] Plasmonic nanoparticles have also been employed to enhance the overall light absorption as well as enable visible light response of the wide bandgap semiconductor oxides.[22-26] The excitation of localized surface plasmon resonances (LSPRs) in the nanoparticles gives rise to great enhancement of the near-field intensity facilitating light

absorption, hot carrier generation and/or plasmon-induced resonant energy transfer (PIRET).[27-28] Hence, various metallic nanoparticles that support LSPRs in the visible wavelength range have been introduced and integrated into the oxide materials showing enhanced photocatalytic performance well correlated with the optical properties of the LSPRs.[29-35] However, the intrinsic loss in the metal nanoparticles is undesirable and unavoidable hindering their wide applications. Alternatively, if we can fashion nanostructures on these photoanodes made from high refractive index oxides, Mie resonances can be excited concentrating the incident light into subwavelength volume while avoiding the ohmic losses that most metallic nanoparticles suffer. The resonances depend on the shape, size and the dielectric environment of the nanoparticles or nanostructures and therefore can be readily tailored in a broad range.[36] These light-trapping nanostructures offer a promising route for photon management applications. In particular, Kim et al. fabricated Fe_2O_3 nanobeam arrays that support different orders of optical resonances and demonstrated photocurrent enhancement up to 3 times.[37] It is noted that large three dimensional nanophotonic structures have also been employed to enhance the light absorption as well as to increase the surface area.[38-39] However, due to the large dimensions of the nanostructures, resonance-like behaviors were not observed.

In this work, we propose to use large-scale ordered ITO/Fe_2O_3 and ITO/Fe_2TiO_5 hybrid nanocone structures to enhance the overall light absorption as well as the near-field light absorption. We developed a three-step dry etching procedure combined with colloidal nanosphere self-assembly to create ordered ITO nanocone arrays. Large-area close-packed monolayers of polystyrene (PS) nanospheres were used to create Cr nanodisks that subsequently act as masks for the crafting of the ITO nanocones with chloride gases. Subsequently, Fe_2O_3 and Fe_2TiO_5 thin films were conformally deposited onto the cones using sputtering techniques forming hybrid nanocones. Such kind of geometry facilitates the carrier transport between the active materials and the ITO electrodes. Furthermore, the nanocone structures can enhance light trapping via the supported optical resonances and the momentum relaxation in the nearfield-driven indirect transition of the Fe_2TiO_5 thin films, photocurrent enhancement up to 31 has been observed in the hybrid nanostructures compared with the planar thin films. The techniques used in this work are all scalable and can be easily upgraded for practical applications.

2. Results and discussions

2.1. Sputtered Fe_2O_3 and Fe_2TiO_5

We deposited Fe_2O_3 or Fe_2TiO_5 thin films using magnetron sputtering and subsequently annealed them in air at 450°C and 550°C, respectively. The sputtered thin films were systematically characterized with x-ray diffraction (XRD) and x-ray photoelectron spectroscopy (XPS). Fig. 1a shows the XRD patterns of the two types of films, both of which show good agreement with the references. In general, Fe_2O_3 shows better crystallinity than Fe_2TiO_5. Almost all the diffraction peaks can be indexed to α-Fe_2O_3 according to PDF card No. 33-0664 except for the peak at 51.2° that may come from the ITO substrate. For Fe_2TiO_5, the diffraction peaks are generally weaker but the majority of the peaks from pseudobrookite Fe_2TiO_5 (PDF No. 09-0182) are observed on the spectrum, confirming the successful physical deposition and formation of iron titanate Fe_2TiO_5 thin films.

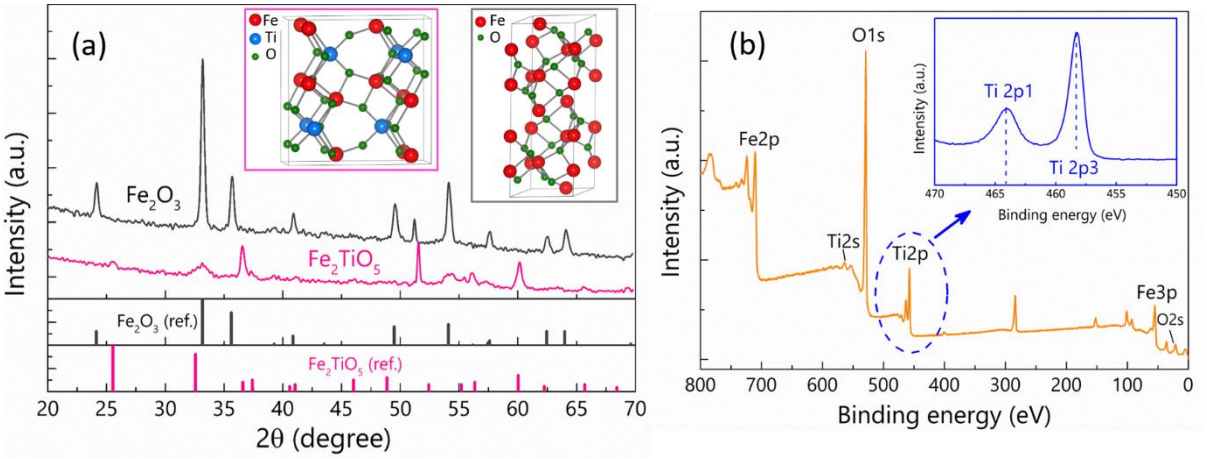

Fig. 1 (a) XRD pattern of the air-annealed Fe_2O_3 and Fe_2TiO_5 thin films. The cartoons in the insets display the crystal structure of Fe_2TiO_5 and Fe_2O_3. (b) XPS spectrum of the Fe_2TiO_5 film. The inset shows the Ti2p spectrum.

Fig. 1b shows the XPS survey spectrum of the annealed Fe_2TiO_5 thin film. The Ti 2p spectrum shows a similar energy position to that of TiO_2, indicating Ti in Fe_2TiO_5 has an oxidation state of Ti^{4+}. The sputtered films show continuous morphology (Fig. S2, Supporting Information) indicating suitability for photocatalysis applications with thin films.

2.2. Fabrication of ITO nanocone arrays

In addition to the sputtering-prepared thin films, we were motivated to construct precisely controlled nanostructures with scalable methods to enhance the performance of the oxide films. To this end, we fabricated ITO nanocones using a combination of nanosphere lithography (also known as colloidal lithography) and plasma dry etching, both of which are scalable. ITO films with thickness ~800 nm were chosen such that the ITO films can still provide good electrical conductivity even after long-time dry etching. The fabrication process

of the hybrid nanocones is illustrated in Fig. 2a. First, a 30-nm-thick Cr thin layer was deposited onto the ITO film via e-beam evaporation. Afterwards, a large-area close-packed monolayer of PS nanospheres was deposited on top of the Cr layer via colloidal self-assembly (panel (ii) in Fig. 1a). The details of the self-assembly process can be found in our previous reports.[40-41] Then a three-step dry etching procedure (panel iii – v) was employed to create the ITO nanocones. First, O_2 plasma was used to shrink the size of the PS spheres (panel iii). Then the etched PS spheres were used as etching masks to create Cr nanodisks using Cl_2 plasma (panel iv). Subsequently, the third etching step was carried out in BCl_3/Cl_2 plasma with the Cr disks as masks for the ITO underneath. Since the BCl_3/Cl_2 plasma can also etch Cr and the corresponding etching rate is smaller than that of ITO, cone-shaped ITO nanostructures are generated (panel v). It is noted that these three etching steps can be readily carried out by changing the etching gases. Finally, Fe_2O_3 or Fe_2TiO_5 thin films were deposited onto the nanocones via sputtering giving rise to hybrid nanocone structures. Fig. 2b and 2c show representative scanning electron microscopy (SEM) images of nanocones before and after Fe_2O_3 sputtering, respectively. Well-defined nanocone arrays are observed in Fig. 2b (30° tilted view). In the Supporting Information, Fig. S3 shows periodic nanocone arrays in a larger scale. As expected, the nanocone arrays are arranged in hexagonal patterns inherited from the monolayers of PS nanospheres and the periodicity of the nanocone is determined by the diameter of the spheres, which is 500 nm for the array shown in Fig. 2b. After deposition of Fe_2O_3, the side surface of the nanocones becomes rougher with tiny extrusions as shown in Fig. 1c (45° tilted view). It is noted that the fabrication techniques used here are all scalable and multiple large-area samples can be produced simultaneously. Furthermore, PS nanospheres with different size are commercially available in large quantity, which can be exploited to create a variety of nanocone arrays with different dimensions and pitches rendering great tunability for the optical resonances of the nanocones. It is noted that the ITO nanocones created here can be readily combined with other photocatalytic materials making this fabrication procedure attractive for various light-harvesting applications.

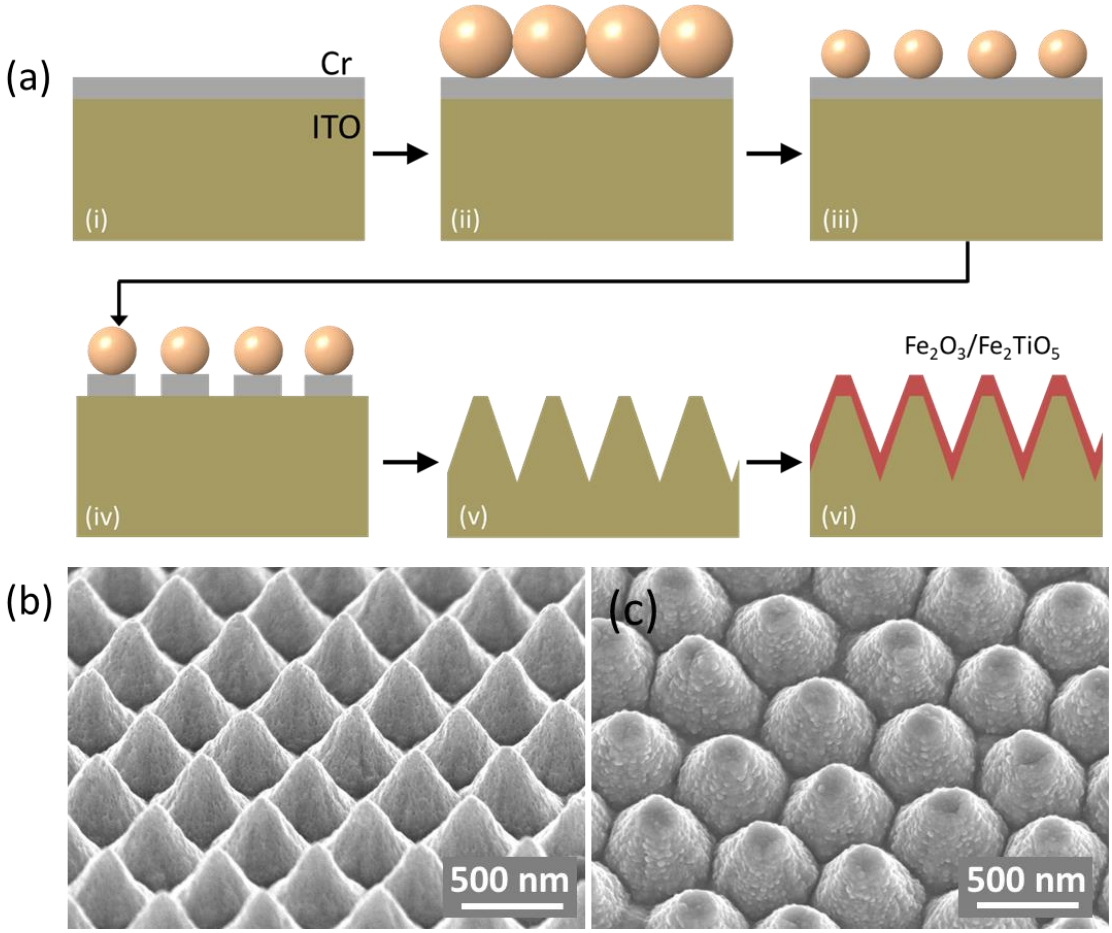

Fig. 2. (a) Illustration (not to scale) of the fabrication process of the ITO\$Fe_2O_3$ (ITO\$Fe_2TiO_5$) nanocones. (i) 30 nm Cr layer was deposited onto the ITO films; (ii) colloidal self-assembly of PS nanospheres; (iii) Shrinking the size of the nanospheres with O_2 plasma etching; (iv) etching of the Cr layer using the etched PS spheres as masks; (v) Creation of ITO nanocones using Cr disks as masks; (vi) deposition of Fe_2O_3 (Fe_2TiO_5) onto the ITO nanocones. (b) SEM image of the ITO nanocones created with 500 nm PS spheres. (c) SEM image of ITO\$Fe_2O_3$ hybrid nanocones created with 500 nm PS spheres.

Fig. 3 shows the transmission UV-Vis spectra of planar Fe_2O_3\$Fe_2TiO_5$ and ITO\$Fe_2O_3$ (ITO\$Fe_2TiO_5$) hybrid nanocones. The ITO nanocones were made using 500 nm PS spheres and the Fe_2O_3\$Fe_2TiO_5$ thin films are 50 nm in thickness. Here the light transmitted through air was used as the reference and the transmission in Fig. 3a represents the light transmitted through the multilayer samples with respect to the reference. The ITO film (~800 nm in thickness) causes interference of the light, which shows up on the spectrum of the planar sample (dashed lines in Fig. 3a) as multiple peaks and troughs, and therefore could not be used as the reference. Nevertheless, enhanced light absorption is clearly observed in Fig. 3 due to the introduction of nanocones, especially in the range from 500 nm to 650 nm.

Multiple sharp dips are superposed onto the spectra. Since the ITO nanocones for both Fe_2O_3 and Fe_2TiO_5 were made from 500 nm PS nanospheres, they expect to exhibit similar optical resonances, which is verified by their transmission spectra (solid lines) in Fig. 3a. The spectral positions of the multiple dips are approximately the same. It is noted that the enhanced absorption in the longer wavelength range is mainly caused by the interference inside the thin films and the photonic resonance modes induced by the nanocone arrays. More analysis on the resonance modes will be provided later in this work. So this enhanced absorption is an optical resonance effect rather than pure material-related absorption as both oxides show negligible absorption in this range (Fig. 3b).

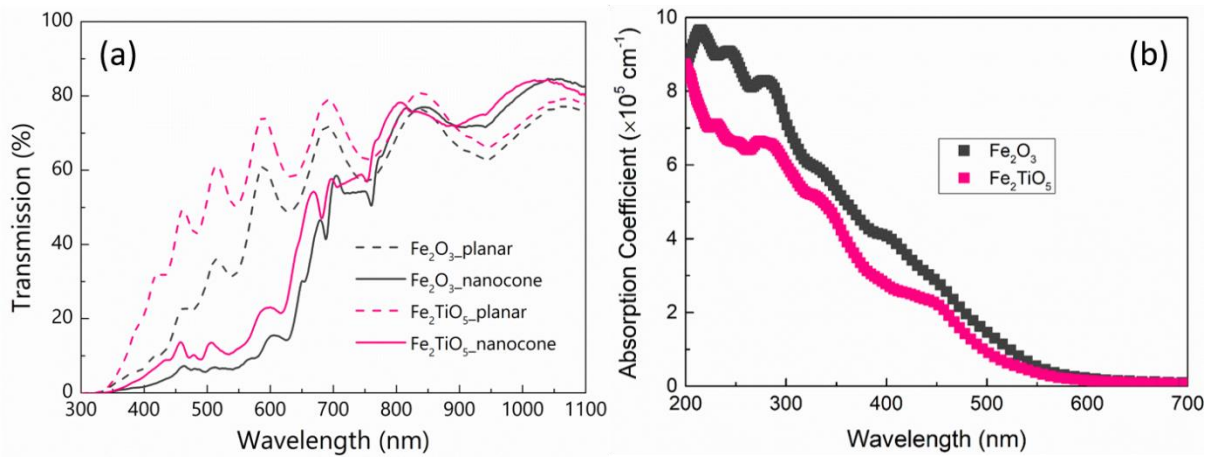

Fig. 3. (a) UV-Vis transmission spectra of Fe_2O_3 and Fe_2TiO_5 thin films (50 nm in thickness) on planar ITO substrate and ITO nanocones. The ITO nanocones were made from 500 nm PS nanospheres. Light transmitted through air was used as the reference. (b) Calculated absorption coefficients of Fe_2O_3 and Fe_2TiO_5 by density-function theory (DFT) calculation.

In Fig. 3a, it is noted that Fe_2TiO_5 absorbs less light than Fe_2O_3, whether it is on the planar ITO substrate or ITO nanocones. We calculated the absorption coefficients of Fe_2TiO_5 and Fe_2O_3 as shown in Fig. 2b for the planar films. The averaged absorption for three different orientations were used to compare with experimental results from polycrystalline film. In Fig. 3b the calculated absorptivity of Fe_2TiO_5 is lower than that of Fe_2O_3 in the visible wavelength, which is consistent with what is observed in Fig. 3a. This is because the direct band gap of Fe_2O_3 is known to be about 2.2 eV (560 nm) and the one for Fe_2TiO_5 is about 3.0 eV (410 nm) leading to the higher absorptivity of Fe_2O_3 in the visible region. The absorption for Fe_2TiO_5 in the longer wavelength range is due to the indirect bandgap transitions as it exhibits an indirect bandgap ~ 2.0 eV.

2.3. Photocurrent enhancement

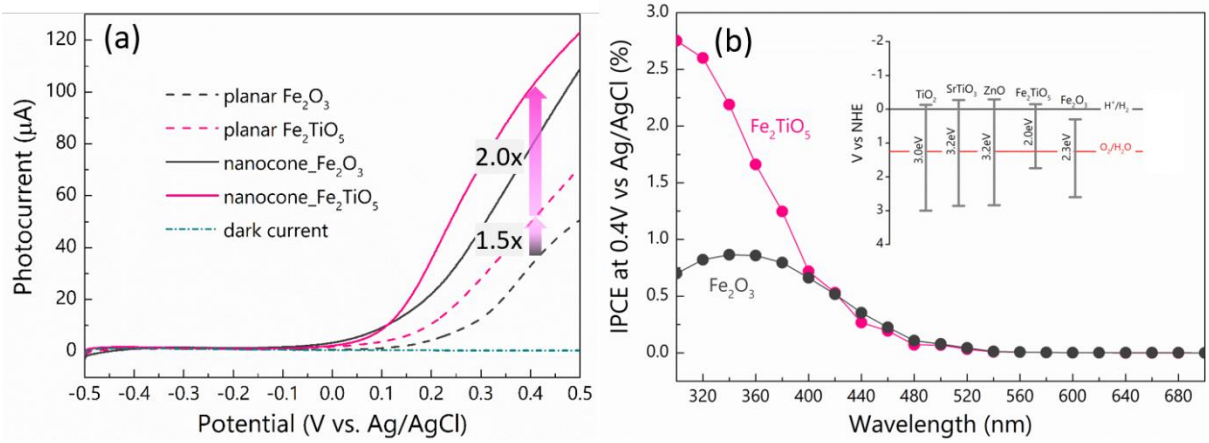

Fig. 4 (a) Anodic photocurrent from 50 nm Fe_2O_3 and Fe_2TiO_5 thin films on planar ITO substrates (dashed lines) and ITO nanocones (solid lines). (b) The dependence of the anodic photocurrent from the planar thin films on the wavelength of the incident light. The inset shows the energy diagram of several common oxide materials for photocatalysis.

We compared the anodic photocurrents from the samples in a home-made three-electrode photoelectrochemical (PEC) cell with a Pt coil as the counter electrode and Ag/AgCl as the reference electrode. Fig. 4a shows the photocurrent from different samples under a potential scan. Surprisingly, the Fe_2TiO_5 thin film, whether it is on a planar or nanocone substrate, exhibits larger anodic photocurrent than the Fe_2O_3 film, which is contrary to the light absorption behaviors of the two materials (Fig. 3). On planar ITO substrates, the photocurrent from Fe_2TiO_5 is 1.5 times larger, at 0.4V vs Ag/AgCl reference, than that from Fe_2O_3 and similar photocurrent enhancement is also observed from those films on ITO nanocones. We further investigated this enhancement by measuring their wavelength-dependent photocurrent and calculated their incident-photon-to-current efficiency (IPCE) spectra as shown in Fig. 4b. The major difference between the two spectra lies in the UV regime (<400 nm), where the IPCE from Fe_2TiO_5 is significantly larger than that from Fe_2O_3. This enhancement is mainly attributed to the onset of direct bandgap transitions in Fe_2TiO_5, whose direct bandgap is ~3 eV. In addition, Fe_2TiO_5 exhibits higher carrier transport than Fe_2O_3 as the effective mass of the electron is smaller in Fe_2TiO_5,[42] which also likely contributes to the higher IPCE values in the Fe_2TiO_5 sample.

It is also shown in Fig. 4a that the introduction of nanocones, covered with either material, leads to 2-fold photocurrent increment mainly due to the enlarged surface area and the enhanced light absorption in the active materials. Based on the SEM images of the nanocones, we calculated the surface area of the nanocone array with a simplified geometrical model (The calculation can be found in the Supporting Information). A surface area increasing

factor of 2.17 was obtained from the modelling consistent with the photocurrent enhancement factor here, demonstrating the enlarged surface area plays a significant role in the total photocurrent enhancement.

To evaluate the nanocone effect as well as the wavelength-dependent behaviors of the photocurrent, we fabricated Fe_2O_3\ITO and Fe_2TiO_5\ITO hybrid nanocones using different sizes of polystyrene nanospheres: 300 (nanocone-300) and 500 nm (nanocone-500). Incident-light-wavelength-dependent photocurrent was collected from the hybrid nanocone samples and compared with the corresponding photocurrent from planar substrates. The enhancement factor is defined as the ratio between the photocurrent from the nanocones and the planar films. The enhancement factors for Fe_2O_3 and Fe_2TiO_5 nanocones are shown in Fig. 5a and 5b, respectively (The raw IPCE curves of the samples are provide in Fig. S4, Supporting Information).

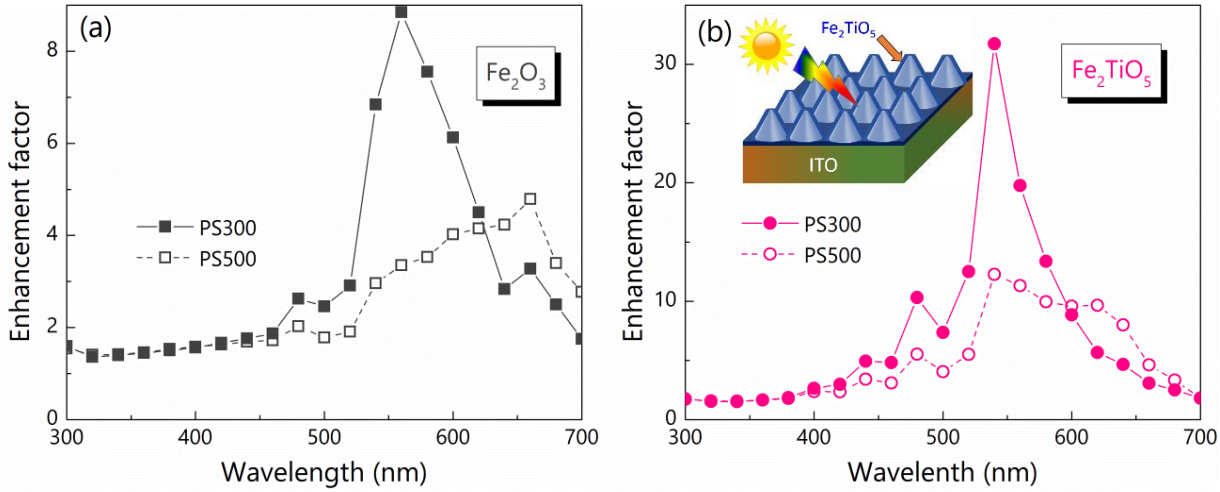

Fig. 5 Experimental anodic photocurrent enhancement spectra for (a) Fe_2O_3 and (b) Fe_2TiO_5 nanocones fabricated using two different sizes of nanospheres: 300 (solid symbol) and 500 nm (hollow symbol). Inset shows the schematic illustration of this hybrid structure.

Both enhancement spectra exhibit similar features: (1) Nanocones made from 300 nm nanospheres show the largest enhancement factors: 31 for Fe_2TiO_5 at 540 nm and 8 for Fe_2O_3 at 560 nm. The enhancement occurs in the similar wavelength range since the nanocones bear similar dimensions. (2) The enhancement factors for Fe_2TiO_5 are much larger than those for Fe_2O_3. As shown in Fig. 3, the absorption coefficients of Fe_2O_3 is larger than those from Fe_2TiO_5 in the wavelength range 350 ~ 600 nm. For the case of resonance-enhanced light absorption, or nearfield-enhanced light absorption, momentum conservation in the interband transitions can be relaxed in contrast to the far-field excitations in the planar systems.

According to our DFT calculation of the electronic structure and our experimental Tauc plot analysis from the UV-Vis transmission spectra, Fe_2TiO_5 exhibits indirect bandgap of 2.0 eV and direct bandgap of 3.0 eV. Here we expect that the indirect electronic transition potentially plays an important role in the photocurrent generation in the visible range i.e. the nanocones can boost the Fe_2TiO_5's indirect transition leading to a higher photocurrent enhancement than for the direct transition in Fe_2O_3 in this wavelength range. (3) For both oxide thin films, the enhancement factors of the nanocone-500 are generally smaller than those from the nanocone-300, which is likely due to the higher light absorption enabled by the subwavelength scale of the nanocone-300 while the larger dimensions of nanocone-500 can result in more scattering and their Mie resonances are expected to arise in the longer wavelength range. (4) In the wavelength range 600 ~ 700 nm, the nanocone-500 exhibits larger enhancement, which can be attributed to the Mie resonances of nanocone-500 in this longer wavelength range as we discuss below.

In order to understand the enhancement spectra shown in Fig. 5, we performed numerical simulations on the hybrid nanocone arrays and the results are shown in Fig. 6. The absorptivity spectra of the nanocone-300 and nanocone-500 with both oxide thin films were shown in Fig. 6b. In general, the nanocones with Fe_2O_3 show larger absorption in the visible range, which is consistent with the results shown in Fig. 3 where Fe_2O_3 exhibits larger absorption coefficients than Fe_2TiO_5 in this range. However, sharp peaks are clearly observed on top of these spectra, especially for nanocone-300 with Fe_2TiO_5 (solid pink line). We attributed these peaks to the Mie resonances and the photonic resonant modes of the hybrid nanocone arrays. As shown in Fig. 2c, the tips of the fabricated nanocones are not very sharp and thus we used truncated nanocones in the simulations (Fig.6a). When the tip diameter *d* increases (Fig.S5, Supporting Information), the absorption spectra of the nanocone arrays show little changes until *d* reaches relatively large values where only the peak intensity shows some variations. By contrast, as we change the nanocone height *h* as shown in Fig.6c, both the peak position and intensity vary accordingly, which indicates that the observed peaks are resonant modes excited in the vertical direction. Similar behavior is also observed for nanocone-500 (Fig.S6, Supporting Information). Furthermore, the narrow resonances (dips on the spectra) change remarkably when the period changes (Fig. 6d) suggesting these photonic modes are excited in the grating-like periodic nanocone arrays. Fig. 6e shows the mode profile at 665 nm for nanocone-500 with Fe_2TiO_5 film clearly confirming the nature of

the modes in the altitudinal direction and also displaying the enhanced near-fields around the nanocone surface.

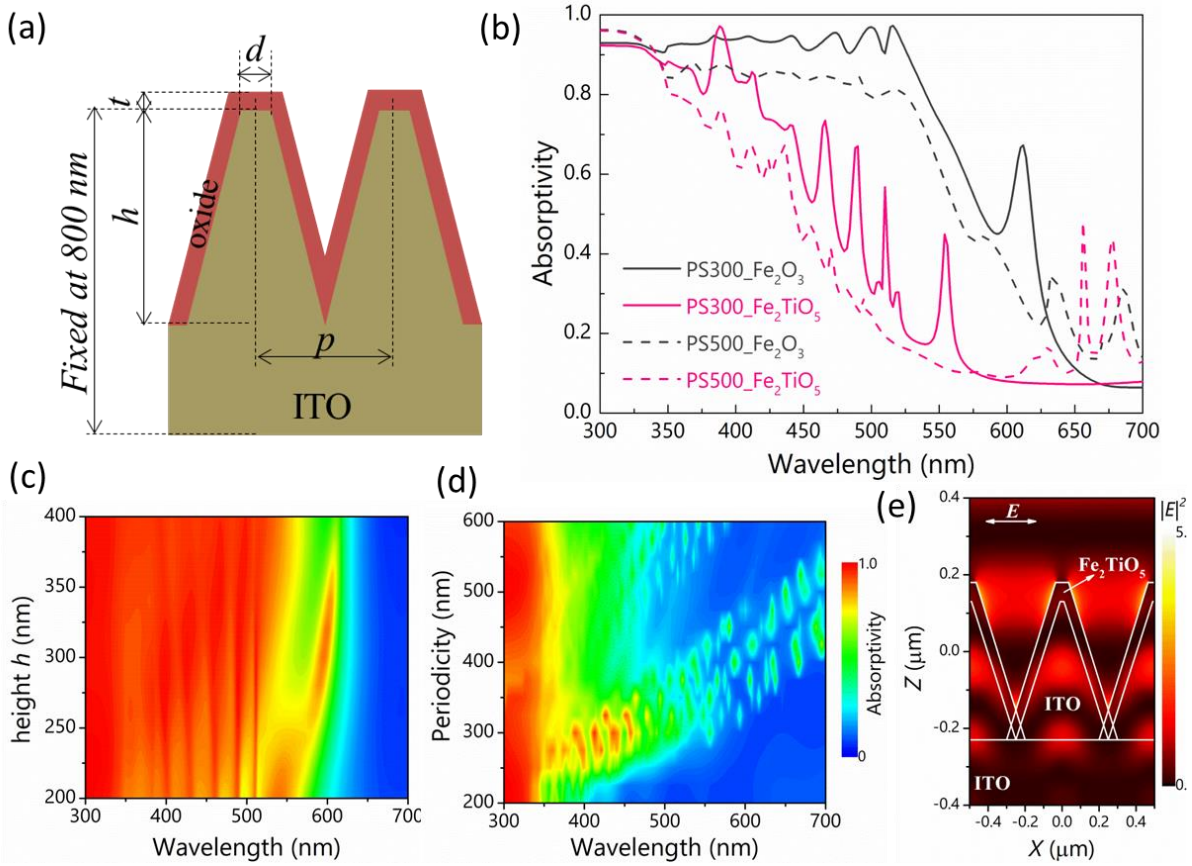

Fig. 6. Numerical simulation of the Mie resonances of the hybrid nanocone arrays fabricated with 300 and 500 nm PS nanospheres. (a) Illustration of the truncated nanocones used in the numerical simulations. (b) The absorptivity spectra of different hybrid nanoce arrays: for nanocone-300, p = 300 nm, h = 300 nm, and d = 50 nm; for nanocone-500, p = 500 nm, h = 360 nm and d = 20 nm. The values were chosen based on the SEM images of the fabricated samples. (c) The relationship between the absorption spectra and the nanocone height h for nanocone-300 with Fe_2O_3. (d) The relationship between the absorption spectra and the period for nanocones with Fe_2TiO_5: d = 50 nm, h = 300 nm. As the period increases, the resonances shift to longer wavelength range. (e) Near-field mode profile at 665 nm for nanocone-500 with Fe_2TiO_5.

In Fig. 5, the largest enhancement occurs at 540 nm for Fe_2TiO_5 and at 560 nm for Fe_2O_3 with nanocone-300, which is consistent with the experimental transmission spectra shown in Fig. 3a. Nanocone-300 with either Fe_2TiO_5 or Fe_2O_3 shows a broad transmission dip in the

range 500~600 nm, where the biggest absorption enhancement occurs. In the numerical simulation as shown in Fig. 6b, a clear resonance peak is observed at 554 nm for nanocone-300 with Fe_2TiO_5 showing good agreement with the experimental results. For nanocone-300 with Fe_2O_3, a clear resonance peak is shown at 610 nm in Fig. 6a. It is also noted that an absorptivity bump is observed at 560 nm in agreement with the photocurrent enhancement observed in Fig. 5. Furthermore, the photocurrent from Fe_2O_3 shows enhancement in the longer wavelength than that from Fe_2TiO_5, which also qualitatively agrees with the numerical simulation results. The discrepancy between the experiments and simulations are likely caused by several factors including the actual dimensions and morphology of the nanocones as well as the quality of the sputtered oxide thin films.

As shown in Fig. 6b, nanocone-500 clearly displays additional resonance peaks in the range of 650 nm compared with nanocone-300. This is consistent with the enhancement spectra shown in Fig. 5, where nanocone-500 shows additional photocurrent enhancement near 650 nm wavelength range confirming that the enhancement can be attributed to the Mie-resonance enhanced light absorption.

It is noted that the enhancement mainly occurs in the visible wavelength range and can be easily integrated with other techniques including co-catalyst and element doping to provide opportunities for visible light photocatalysis. Furthermore, nanoresonators with multiple Mie resonances in a broad wavelength range including UV can be designed and fabrication leading to better performance, which is currently being explored.

3. Conclusions

In summary, we have compared the photocatalytic performance of Fe_2O_3 and Fe_2TiO_5 thin film prepared by sputtering method. Furthermore, we proposed and fabricated large-area ITO nanocone arrays using scalable colloidal lithography and dry etching. The ITO nanocone platform greatly improves the overall solar light absorption across a broad wavelength range together with enlarged surface area leading to overall photocurrent enhancement. The hybrid nanocones also support Mie resonances giving rise to the enhanced near-field and thus naturally lead to the enhanced light absorption in the oxide catalyst layers, especially in the Fe_2TiO_5 layer via momentum relaxation of the indirect band transitions. The nanofabrication technique is scalable and cost-effective. Our proposed ITO nanocone arrays can be easily combined with other photocatalytic materials as well as other functional materials making them attractive for a wide range of applications based on solar energy harvesting.

4. Experiments and methods

Preparation of Fe_2O_3 and Fe_2TiO_5 thin films: Magnetron-sputtering was used to prepare the 50 nm thick Fe_2O_3 and Fe_2TiO_5 films. We prepared several oxide thin films on Si substrates with different sputtering times. Their thickness was determined with SEM cross-section method and the sputtering rate is thus obtained. The samples were then prepared by controlling the sputtering time to achieve 50 nm thin film coating. The sputtering targets were obtained from Furuchi Chemical Co.. Pure Ar gas was used and the flow rate was kept at 20 sccm. RF power of 50 W was used to excite the Ar plasma (i-Miller CFS-4EP-LL, Shibaura). The substrates were spinning at 20 rpm/min during sputtering at room temperature. Afterwards, the Fe_2O_3 thin films were annealed in air at 450 °C for 1 hour while the Fe_2TiO_5 films were annealed in air at 550 °C for 1 hour (Quartz tube furnace, Koyo Thermo Systems).

Fabrication of ITO nanocones: the ITO nanocone arrays were fabricated by a combination of colloidal lithography and dry etching. First, a thin Cr layer of 30 nm was deposited onto 800 nm thick ITO films on quartz substrates. Then monolayer of polystyrene nanospheres (300 or 500 nm in diameter, Thermo Fisher Scientific Inc.) were deposited on top of the Cr layers via colloidal self-assembly as described in previous work. Afterwards, O_2 plasma was used to reduce the size of the nanospheres (20 sccm, RF power 200 W, bias power 5 W, Ulvac CE-300I) followed by creating Cr nanodisks with the reduced nanospheres as etching masks. Finally, the Cr nanodisks were used as masks to etch the underneath ITO with Cl_2 and BCl_3 gases (16 sccm Cl_2/4 sccm BCl_3, RF power 200W, bias power 20 W). During the etching process, the Cr nanodisks were also subjected to etch and therefore cone-shaped nanostructures were created in the ITO substrates.

Characterization and measurements: SEM images of the samples were obtained using a Hitachi microscope (SU8230). The crystallographic patterns of the thin films were acquired by X-ray diffraction (XRD, Rigaku Smartlab) with Cu Kα as the radiation source. XPS analysis was performed in a Quantera SXM model (ULVAC-PHI Inc.) in the standard confguration. Spectra were acquired using a monochromatic Al Kα X-ray source operating at 100 W ata base pressure of 10^{-7} Pa. The measurements were conducted at the takeoff angle of 45° with respect to the surface normal.

For the photoelectrochemical (PEC) measurements, the photocurrent was measured using a three-electrode system with a homemade reactor coupled with a quartz window. In this

system, we used Ag/AgCl (saturated in KCl) as the reference electrode (RE), Pt wire as the counter electrode (CE), and the fabricated sample as the working electrode (WE). Measurements were performed in 1 M NaOH (pH = 13.7) electrolyte. A potentiostat (VersaSTAT 4 Potentiostat Galvanostat) was utilized to simultaneously control the voltage between WE and RE and collect the current between WE and CE. A solar simulator (XES-40S1, San-Ei Electric) with Air Mass value of 1.5 G (100 mW/cm^2) was employed to emit the light through the quartz window onto the front side of sample. To evaluate the wavelength-dependent incident photon-to-electron conversion efficiency (IPCE), tunable wavelength light source (BUNKOUKEIKI, NIJI-2) with wavelength ranging from 340 to 800 nm was used.

DFT calculation: The calculation is based on the Vienna ab Initio Simulation Package (VASP) code.[43-44] The exchange-correlation was treated within the generalized gradient approximation (GGA) Perdew-Burke-Ernzerhof (PBE) functional. An energy cut-off of 520 eV based on the plane-wave basis was used for all calculations. We firstly optimized the primitive cells of Fe_2O_3 (rhombohedral) and Fe_2TiO_5 (orthorhombic) using Monkhrost-Pack scheme with a 10 × 10 × 10 and 11 × 4 × 4 **k**-points grid, respectively.[45] The structural optimization is obtained until the force on each atom is less than 0.005 eV/Å. By employing DFT + U method (U = 4.3 eV for Fe 3d orbitals),[46-47] we obtained the band gap of 1.95 eV for Fe_2TiO_5. In the case of Fe_2O_3, the calculated band gaps of bulk Fe_2O_3 is 2.25 eV. These bandgaps agree well with the experiments (2.0 – 2.2 eV for Fe_2O_3[48] and 2.18 eV for Fe_2TiO_5[49]). The frequency-dependent dielectric response was calculated using the independent particle approximation (IPA).[50] The complex dielectric function has the form: $\varepsilon(\omega) = \varepsilon_1(\omega) + i\varepsilon_2(\omega)$. Due to the anisotropic properties of Fe_2O_3 and Fe_2TiO_5, we calculated the average dielectric functions, $\varepsilon_1(\omega) = [\varepsilon_1^{xx}(\omega) + \varepsilon_1^{yy}(\omega) + \varepsilon_1^{zz}(\omega)]/3$ and $\varepsilon_2(\omega) = [\varepsilon_2^{xx}(\omega) + \varepsilon_2^{yy}(\omega) + \varepsilon_2^{zz}(\omega)]/3$. Once real part ($\varepsilon_1$) and imaginary part ($\varepsilon_2$) of the dielectric function are known, the absorption coefficient was calculated directly from the dielectric function: $\alpha(\omega) = (\sqrt{2\omega^2}/c)\left[\sqrt{\varepsilon_1^2(\omega) + \varepsilon_2^2(\omega)} - \varepsilon_1(\omega)\right]^{1/2}$, where c is the speed of light. It is noted that within simple IPA model, the local-field effects, spin-orbit coupling effects, and exciton are not taken into account in the calculation.

Numerical simulations: The simulated absorptivities of the nanocone arrays were performed using the rigorous coupled-wave analysis (RCWA) (DiffractMOD, RSoft, Synopsys) and the electric field distribution was calculated with a full-wave simulation based on the finite-

difference time-domain (FDTD) method. The dielectric constants of ITO, Fe_2O_3 and Fe_2TiO_5 used in the simulations were retrieved from spectroscopic ellipsometry measurements. The model of nanocones arrays were performed in a CAD layout (RSoft CAD Layout) with a periodic hexagonal lattice. In the full-wave simulation, periodic boundary condition was applied on both *X* and *Y* axes; and perfectly matched layers were applied on both directions of the *Z* axis; a grid size of 2 nm was chosen for both three axes. During the simulations, the excitation electromagnetic field propagates along the -*Z* axis and the electric field oscillates along the *X* axis. The amplitude of the incident field was normalized to 1.

Acknowledgements

T.N. acknowledges the support from CREST under the project of "Phase Interface Science for Highly Efficient Energy Utilization" (JPMJCR13C3, Japan Science and Technology Agency). K.C. and X.P.L acknowledge the support from the Guangdong Provincial Innovation and Entrepreneurship Project (Grant No. 2016ZT06D081). T.N. acknowledges technical supports and discussions from S. L. Shinde. K.C. and T.N. also acknowledge the support from JSPS KAKENHI Grant Numbers 16H06364 and 16K21601.

References

1. Kudo, A.; Miseki, Y., Heterogeneous photocatalyst materials for water splitting. *Chem. Soc. Rev.* **2009,** *38* (1), 253-278.
2. Li, Z.; Luo, W.; Zhang, M.; Feng, J.; Zou, Z., Photoelectrochemical cells for solar hydrogen production: current state of promising photoelectrodes, methods to improve their properties, and outlook. *Energy & Environmental Science* **2013,** *6* (2), 347-370.
3. Hua, T.; Shuxin, O.; Yingpu, B.; Naoto, U.; Mitsutake, O.; Jinhua, Y., Nano‐photocatalytic Materials: Possibilities and Challenges. *Adv. Mater.* **2012,** *24* (2), 229-251.
4. Abraham, W.; A., S. W.; R., K. T.; Yiping, Z.; Z., Z. J., Photoelectrochemical Water Splitting Using Dense and Aligned TiO2 Nanorod Arrays. *Small* **2009,** *5* (1), 104-111.
5. Ueno, K.; Misawa, H., Plasmon-enhanced photocurrent generation and water oxidation from visible to near-infrared wavelengths. *Npg Asia Materials* **2013,** *5*, e61.
6. Zhao, J.; Guo, Y.; Cai, L.; Li, H.; Wang, K. X.; Cho, I. S.; Lee, C. H.; Fan, S.; Zheng, X., High-Performance Ultrathin BiVO4 Photoanode on Textured Polydimethylsiloxane Substrates for Solar Water Splitting. *ACS Energy Letters* **2016,** *1* (1), 68-75.
7. Kim, J. K.; Shi, X.; Jeong, M. J.; Park, J.; Han, H. S.; Kim, S. H.; Guo, Y.; Heinz, T. F.; Fan, S.; Lee, C.-L.; Park, J. H.; Zheng, X., Enhancing Mo:BiVO4 Solar Water Splitting with Patterned Au Nanospheres by Plasmon-Induced Energy Transfer. *Advanced Energy Materials* **2018,** *8* (5), 1701765-n/a.
8. Le Formal, F.; Grätzel, M.; Sivula, K., Controlling Photoactivity in Ultrathin Hematite Films for Solar Water-Splitting. *Adv. Funct. Mater.* **2010,** *20* (7), 1099-1107.
9. Kevin, S.; Florian, L. F.; Michael, G., Solar Water Splitting: Progress Using Hematite (α‐Fe2O3) Photoelectrodes. *ChemSusChem* **2011,** *4* (4), 432-449.

10. Shen, S.; Lindley, S. A.; Chen, X.; Zhang, J. Z., Hematite heterostructures for photoelectrochemical water splitting: rational materials design and charge carrier dynamics. *Energy & Environmental Science* **2016,** *9* (9), 2744-2775.
11. Sivula, K.; Zboril, R.; Le Formal, F.; Robert, R.; Weidenkaff, A.; Tucek, J.; Frydrych, J.; Grätzel, M., Photoelectrochemical Water Splitting with Mesoporous Hematite Prepared by a Solution-Based Colloidal Approach. *J. Am. Chem. Soc.* **2010,** *132* (21), 7436-7444.
12. Wheeler, D. A.; Wang, G.; Ling, Y.; Li, Y.; Zhang, J. Z., Nanostructured hematite: synthesis, characterization, charge carrier dynamics, and photoelectrochemical properties. *Energy & Environmental Science* **2012,** *5* (5), 6682-6702.
13. Shen, S.; Kronawitter, C. X.; Jiang, J.; Mao, S. S.; Guo, L., Surface tuning for promoted charge transfer in hematite nanorod arrays as water-splitting photoanodes. *Nano Research* **2012,** *5* (5), 327-336.
14. Tamirat, A. G.; Rick, J.; Dubale, A. A.; Su, W.-N.; Hwang, B.-J., Using hematite for photoelectrochemical water splitting: a review of current progress and challenges. *Nanoscale Horizons* **2016,** *1* (4), 243-267.
15. Liu, Q.; He, J.; Yao, T.; Sun, Z.; Cheng, W.; He, S.; Xie, Y.; Peng, Y.; Cheng, H.; Sun, Y.; Jiang, Y.; Hu, F.; Xie, Z.; Yan, W.; Pan, Z.; Wu, Z.; Wei, S., Aligned Fe2TiO5-containing nanotube arrays with low onset potential for visible-light water oxidation. *Nature Communications* **2014,** *5*, 5122.
16. Bassi, P. S.; Chiam, S. Y.; Gurudayal; Barber, J.; Wong, L. H., Hydrothermal Grown Nanoporous Iron Based Titanate, Fe2TiO5 for Light Driven Water Splitting. *ACS Applied Materials & Interfaces* **2014,** *6* (24), 22490-22495.
17. Deng, J.; Lv, X.; Liu, J.; Zhang, H.; Nie, K.; Hong, C.; Wang, J.; Sun, X.; Zhong, J.; Lee, S.-T., Thin-Layer Fe2TiO5 on Hematite for Efficient Solar Water Oxidation. *ACS Nano* **2015,** *9* (5), 5348-5356.
18. Ngo, H. D.; Ngo, T. D.; Tamanai, A.; Chen, K.; Cuong, N. T.; Handegard, O. S.; Pucci, A.; Umezawa, N.; Nabatame, T.; Nagao, T., Structure and optical properties of sputter deposited pseudobrookite Fe2TiO5 thin films. *CrystEngComm* **2019,** *21* (1), 34-40.
19. Shen, S.; Guo, P.; Wheeler, D. A.; Jiang, J.; Lindley, S. A.; Kronawitter, C. X.; Zhang, J. Z.; Guo, L.; Mao, S. S., Physical and photoelectrochemical properties of Zr-doped hematite nanorod arrays. *Nanoscale* **2013,** *5* (20), 9867-9874.
20. Yang, X.; Liu, R.; Du, C.; Dai, P.; Zheng, Z.; Wang, D., Improving Hematite-based Photoelectrochemical Water Splitting with Ultrathin TiO2 by Atomic Layer Deposition. *ACS Applied Materials & Interfaces* **2014,** *6* (15), 12005-12011.
21. Kronawitter, C. X.; Vayssieres, L.; Shen, S.; Guo, L.; Wheeler, D. A.; Zhang, J. Z.; Antoun, B. R.; Mao, S. S., A perspective on solar-driven water splitting with all-oxide hetero-nanostructures. *Energy & Environmental Science* **2011,** *4* (10), 3889-3899.
22. Warren, S. C.; Thimsen, E., Plasmonic solar water splitting. *Energy & Environmental Science* **2012,** *5* (1), 5133-5146.
23. Xuming, Z.; Yu Lim, C.; Ru-Shi, L.; Din Ping, T., Plasmonic photocatalysis. *Rep. Prog. Phys.* **2013,** *76* (4), 046401.
24. Linic, S.; Christopher, P.; Ingram, D. B., Plasmonic-metal nanostructures for efficient conversion of solar to chemical energy. *Nature Materials* **2011,** *10*, 911.
25. Bao, Z. Y.; Liu, X.; Dai, J.; Wu, Y.; Tsang, Y. H.; Lei, D. Y., In situ SERS monitoring of photocatalytic organic decomposition using recyclable TiO2-coated Ag nanowire arrays. *Appl. Surf. Sci.* **2014,** *301*, 351-357.
26. Wu, B.-H.; Liu, W.-T.; Chen, T.-Y.; Perng, T.-P.; Huang, J.-H.; Chen, L.-J., Plasmon-enhanced photocatalytic hydrogen production on Au/TiO2 hybrid nanocrystal arrays. *Nano Energy* **2016,** *27*, 412-419.
27. Li, J.; Cushing, S. K.; Meng, F.; Senty, T. R.; Bristow, A. D.; Wu, N., Plasmon-induced resonance energy transfer for solar energy conversion. *Nature Photonics* **2015,** *9*, 601.
28. Cushing, S. K.; Wu, N., Progress and Perspectives of Plasmon-Enhanced Solar Energy Conversion. *The Journal of Physical Chemistry Letters* **2016,** *7* (4), 666-675.
29. Gao, H.; Liu, C.; Jeong, H. E.; Yang, P., Plasmon-Enhanced Photocatalytic Activity of Iron Oxide on Gold Nanopillars. *ACS Nano* **2012,** *6* (1), 234-240.

30. Li, J.; Cushing, S. K.; Zheng, P.; Meng, F.; Chu, D.; Wu, N., Plasmon-induced photonic and energy-transfer enhancement of solar water splitting by a hematite nanorod array. *Nature Communications* **2013,** *4*, 2651.
31. Sugavaneshwar, R. P.; Chen, K.; Lakshminarayana, G.; Ishii, S.; Dao, T. D.; Umezawa, N.; Nagao, T., Plasmon mediated cathodic photocurrent generation in sol-gel synthesized doped SrTiO3 nanofilms. *APL Materials* **2015,** *3* (11), 116103.
32. Yuqing, Z.; Kosei, U.; Yuko, M.; Xu, S.; Tomoya, O.; Kei, M.; Haruo, I.; Hiroaki, M., Plasmon‐Assisted Water Splitting Using Two Sides of the Same SrTiO3 Single‐Crystal Substrate: Conversion of Visible Light to Chemical Energy. *Angew. Chem.* **2014,** *126* (39), 10518-10522.
33. Nishijima, Y.; Ueno, K.; Yokota, Y.; Murakoshi, K.; Misawa, H., Plasmon-Assisted Photocurrent Generation from Visible to Near-Infrared Wavelength Using a Au-Nanorods/TiO2 Electrode. *The Journal of Physical Chemistry Letters* **2010,** *1* (13), 2031-2036.
34. Shi, X.; Ueno, K.; Takabayashi, N.; Misawa, H., Plasmon-Enhanced Photocurrent Generation and Water Oxidation with a Gold Nanoisland-Loaded Titanium Dioxide Photoelectrode. *J. Phys. Chem. C* **2013,** *117* (6), 2494-2499.
35. Dao, T. D.; Han, G.; Arai, N.; Nabatame, T.; Wada, Y.; Hoang, C. V.; Aono, M.; Nagao, T., Plasmon-mediated photocatalytic activity of wet-chemically prepared ZnO nanowire arrays. *Phys. Chem. Chem. Phys.* **2015,** *17* (11), 7395-7403.
36. Brongersma, M. L.; Cui, Y.; Fan, S., Light management for photovoltaics using high-index nanostructures. *Nature Materials* **2014,** *13*, 451.
37. Kim, S. J.; Thomann, I.; Park, J.; Kang, J.-H.; Vasudev, A. P.; Brongersma, M. L., Light Trapping for Solar Fuel Generation with Mie Resonances. *Nano Lett.* **2014,** *14* (3), 1446-1452.
38. Li, J.; Qiu, Y.; Wei, Z.; Lin, Q.; Zhang, Q.; Yan, K.; Chen, H.; Xiao, S.; Fan, Z.; Yang, S., A three-dimensional hexagonal fluorine-doped tin oxide nanocone array: a superior light harvesting electrode for high performance photoelectrochemical water splitting. *Energy & Environmental Science* **2014,** *7* (11), 3651-3658.
39. Mi, Y.; Wen, L.; Xu, R.; Wang, Z.; Cao, D.; Fang, Y.; Lei, Y., Constructing a AZO/TiO2 Core/Shell Nanocone Array with Uniformly Dispersed Au NPs for Enhancing Photoelectrochemical Water Splitting. *Advanced Energy Materials* **2016,** *6* (1), 1501496-n/a.
40. Chen, K.; Rajeeva, B. B.; Wu, Z.; Rukavina, M.; Dao, T. D.; Ishii, S.; Aono, M.; Nagao, T.; Zheng, Y., Moiré Nanosphere Lithography. *ACS Nano* **2015,** *9* (6), 6031-6040.
41. Chen, K.; Dao, T. D.; Ishii, S.; Aono, M.; Nagao, T., Infrared Aluminum Metamaterial Perfect Absorbers for Plasmon-Enhanced Infrared Spectroscopy. *Adv. Funct. Mater.* **2015,** *25* (42), 6637-6643.
42. Petit, S.; Melissen, S. T. A. G.; Duclaux, L.; Sougrati, M. T.; Le Bahers, T.; Sautet, P.; Dambournet, D.; Borkiewicz, O.; Laberty-Robert, C.; Durupthy, O., How Should Iron and Titanium be Combined in Oxides to Improve Photoelectrochemical Properties? *J. Phys. Chem. C* **2016,** *120* (43), 24521-24532.
43. Kresse, G.; Furthmüller, J., Efficient iterative schemes for ab initio total-energy calculations using a plane-wave basis set. *Physical Review B* **1996,** *54* (16), 11169-11186.
44. Kresse, G.; Furthmüller, J., Efficiency of ab-initio total energy calculations for metals and semiconductors using a plane-wave basis set. *Computational Materials Science* **1996,** *6* (1), 15-50.
45. Pack, J. D.; Monkhorst, H. J., "Special points for Brillouin-zone integrations"---a reply. *Physical Review B* **1977,** *16* (4), 1748-1749.
46. Dudarev, S. L.; Botton, G. A.; Savrasov, S. Y.; Humphreys, C. J.; Sutton, A. P., Electron-energy-loss spectra and the structural stability of nickel oxide: An LSDA+U study. *Physical Review B* **1998,** *57* (3), 1505-1509.
47. Mosey, N. J.; Liao, P.; Carter, E. A., Rotationally invariant ab initio evaluation of Coulomb and exchange parameters for DFT+U calculations. *The Journal of Chemical Physics* **2008,** *129* (1), 014103.
48. Merchant, P.; Collins, R.; Kershaw, R.; Dwight, K.; Wold, A., The electrical, optical and photoconducting properties of Fe2−xCrxO3 ($0 \leqslant x \leqslant 0.47$). *J. Solid State Chem.* **1979,** *27* (3), 307-315.
49. Ginley, D. S.; Butler, M. A., The photoelectrolysis of water using iron titanate anodes. *J. Appl. Phys.* **1977,** *48* (5), 2019-2021.

50. Gajdoš, M.; Hummer, K.; Kresse, G.; Furthmüller, J.; Bechstedt, F., Linear optical properties in the projector-augmented wave methodology. *Physical Review B* **2006,** *73* (4), 045112.

Graphical Abstract